Adjusting the Néel relaxation time of Fe₃O₄/ZnₓCo₁₋ₓFe₂O₄ core/shell nanoparticles for optimal heat generation in magnetic hyperthermia

Fernando Fabris[a], Javier Lohr[a,b], Enio Lima Jr.[a], Adriele Aparecida de Almeida[a], Horacio E. Troiani[c], Luis M. Rodríguez[a], Marcelo Vásquez Mansilla[a], Myriam H. Aguirre[d,e], Gerardo F. Goya[e], Daniele Rinaldi[f], Alberto Ghirri[g], Davide Peddis[h], Dino Fiorani[h], Roberto D. Zysler[a,i], Emilio De Biasi[a,i,*] and Elin L. Winkler[a,i,*]

[a] Instituto de Nanociencia y Nanotecnología CNEA-CONICET – Centro Atómico Bariloche, S. C. de Bariloche, 8400, Argentina
[b] Laboratorio Argentino de Haces de Neutrones – CNEA- Argentina
[c] Laboratorio de Caracterización de Materiales y Óxidos No-Estequiométricos, Gerencia de Investigación Aplicada, Centro Atómico Bariloche, S. C. de Bariloche, 8400, Argentina
[d] Instituto de Ciencias de Materiales de Aragón & Laboratorio de Microscopías Avanzadas, Universidad de Zaragoza, Mariano Esquillor s/n, Zaragoza, 50018, Spain
[e] Instituto de Nanociencias y Materiales de Aragón & Dep. Física de la Materia Condensada, Universidad de Zaragoza, Mariano Esquillor s/n, Zaragoza, 50018, Spain
[f] Department of Materials, Environmental Sciences and Urban Planning (SIMAU), Università Politecnica delle Marche, 60131 Ancona, Italy
[g] Istituto Nanoscienze, CNR, via Campi 213/a, I-41125 Modena, Italy
[h] Istituto di Struttura della Materia, CNR, Area della Ricerca di Roma 1, C.P. 10, I-00015 Monterotondo Stazione, Rome, Italy
[i] Instituto Balseiro- Universidad Nacional de Cuyo.

* Corresponding Authors: debiasi@cab.cnea.gov.ar and winkler@cab.cnea.gov.ar.

Keywords: core/shell nanoparticles, bi-magnetic nanoparticles, effective magnetic anisotropy, magnetic fluid hyperthermia, Néel relaxation time.

ABSTRACT

In this work it is shown a precise way to optimize the heat generation in high viscosity magnetic colloids, by adjusting the Néel relaxation time in core/shell bimagnetic nanoparticles, for Magnetic Fluid Hyperthermia applications. To pursue this goal, Fe₃O₄/ZnₓCo₁₋ₓFe₂O₄ core/shell nanoparticles were synthesized with 8.5 nm mean core diameter, encapsulated in a shell of ~1.1 nm of thickness, where the Zn atomic ratio (Zn/(Zn+Co) at%) changes from 33 at% to 68 at%. The magnetic measurements are consistent with a rigid interface coupling between the core and shell phases, where the effective magnetic anisotropy systematically decreases when the Zn concentration increases, without a significant change of the saturation magnetization. Experiments of magnetic fluid hyperthermia of 0.1 wt% of these particles dispersed in water, in Dulbecco modified Eagles minimal essential medium, and a high viscosity butter oil, result in a large specific loss power (SLP), up to 150 W/g, when the experiments are performed at 571 kHz and 200 Oe. The SLP was optimized adjusting the shell composition, showing a maximum for intermediate Zn concentration. This study shows a way to maximize the heat generation in viscous media like cytosol, for those biomedical applications that requiere smaller particle sizes .

1.Introduction

Magnetic fluid hyperthermia (MFH) is a promising technique for new cancer therapies based on the use of magnetic nanomaterials. In its simplest form, magnetic nanoparticles provoke the death of tumour cells by increasing the local temperature, therefore improving the cytotoxic effects of radiotherapy and chemotherapy.[1–3] The heating of targeted tumours in MFH is obtained through the magnetic losses of magnetic nanoparticles (MNPs) exposed to alternating magnetic fields. The magnetic losses are originated from the phase shift between the nanoparticle's magnetic moment and the applied AC magnetic field, and the magnetic relaxation dynamics depends on the relaxation time of two concurrent mechanisms.[4] One of them, called mechanical or Brown mechanism, is the physical rotation of the MNPs characterized by the time relaxation τ_B, that is given by:

$$\tau_B = \frac{3\eta V_{hyd}}{k_B T} \qquad (1)$$

where η is the viscosity of the medium, V_{hyd} the hydrodynamic volume of the MNPs and $k_B T$ the thermal energy. The second mechanism involves the inversion of magnetic moment within the crystal lattice and is called magnetic or Néel mechanism. The Néel mechanism is well described for non-interacting and monodomain MNPs by the Néel relaxation time, τ_N, given by:

$$\tau_N = \tau_0\, exp(K_{eff} V_{mag}/k_B T) \qquad (2)$$

where K_{eff} and V_{mag} are the effective anisotropy and magnetic volume of the single-domain NPs, respectively, and τ_0 is the attempt relaxation time of the system (typically between 10^{-9}-10^{-11} s).[5] In any given situation, the dominating relaxation process will be the one with the shorter relaxation time. For systems with large magnetic anisotropy energy and/or low viscosity, the Brown mechanism dominates, whereas Néel mechanism governs in the opposite situation.[6]

Despite the promising results, MFH has not been yet incorporated into current oncological protocols mainly due to three factors: *i*) the low values of specific loss power (SLP) attained so far, *ii*) the cytotoxicity effects of the MNPs and iii) the large variability of SLP values even for different batches of colloids synthesized by the same methods. The low SLP values result in the need of high local concentration of MNPs, which increases the cytotoxicity and reduces the specificity of the therapy due to undesired apoptosis of surrounding healthy tissues [7,8]. Considerable efforts have been invested to develop more efficient nano-heaters, and thus current experimental research in the area of MFH is focused on the improvement of the heating power through the control of the morphological[9–13], magnetic[14–18], surface chemistry[19] and spatial-assembling[20–22] properties of the MNPs. Regarding the second factor, i.e. the lack of reproducibility of MNPs heating properties, the challenge is related to the variability of SLP when experiments are performed in different liquid media (solution, cell culture or *in vivo),* due to the influence of the different liquid viscosities on the SLP. The high viscosity of the cellular environment is expected to hinder/block Brown relaxation and, as a consequence, the heat generation is usually reduced in systems where this mechanism is dominant.[15,23–29]

Therefore, it is crucial to tune individual parameters that control the magnetic relaxation mechanisms in order to optimize the SLP in a medium that simulates the viscosity of the cellular environment. A very effective way to obtain this fine control on the magnetic

relaxation in MNPs is the design and fabrication of bi-magnetic rigidly coupled core/shell nanoparticles composed of hard and soft magnetic materials. The magnetic exchange coupling at the interface between the core and shell results in a system with effective anisotropy different from those of both phases.[30–36] Thus, it is possible to adjust precisely the magnetic anisotropy of the soft-hard core-shell NPs by changing the composition of one of the two phases and preserving the size, morphology and high values of magnetization.[37]

In a previous work, we have shown that is possible to select the dominant magnetic relaxation mechanism of heat generation between Brown or Néel ones by changing the composition of the shell in $Fe_3O_4/Zn_xCo_{1-x}Fe_2O_4$ NPs.[38] In this work, we selected the Néel mechanism in viscous media, due to its relevance in biological applications, and we maximize the heat generation by tuning the composition of the shell of the MNPs. We showed that by changing the zinc fraction of the $Zn_xCo_{1-x}Fe_2O_4$, the magnetic anisotropy and therefore the magnetic relaxation can be tuned, resulting in larger values of SLP. We explored highly viscous media including butter oil, water and DMEM (Dulbecco modified Eagles minimal essential medium). These results show the potential of core/shell systems for the development of nanoparticles with specific characteristics for cellular environmental conditions.

2. Material and methods

2.1 Synthesis of Fe$_3$O$_4$ core: The magnetic core/shell nanoparticles were synthesized by seed-mediated thermal decomposition of organo-metallic precursors at high temperature based in the literature.[37,38] Firstly, Fe_3O_4 core is synthesized from Fe(III) acetylacetonate (12 mMol) in presence of 1,2-octanediol (24 mMol), Oleic acid (12 mMol), Oleylamine (30 mMol) and Benzyl ether (190 mMol) as solvent. This solution is heated at 473 K during 20 minutes under N_2 flow (0.1 mL/min.) and intense mechanical stirring. After that, the solution was heated until the reflux condition (563 K) with a heating rate of 15 K/min. The solution was kept in reflux during 60 min.

2.2 Synthesis of Fe$_3$O$_4$/Zn$_x$Co$_{1-x}$Fe$_2$O$_4$ MNPs: A fraction of 8.2 mL of the solution obtained from the core synthesis was mixed in 220 mMol of Benzyl ether, 4.5 mMol of 1,2-octanediol, 3 mMol of Oleic acid, 3 mMol of Oleylamine in the presence of 1.2 mMol of Fe(III) acetylacetonate, $x \times 0.6$ mMol of Zn(II) acetylacetonate and $(1-x) \times 0.6$ mMol of Co(II) acetylacetonate. The synthesis procedure used was the same used for the core. In total, 6 samples with the values of x = 0.40, 0.50, 0.60, 0.68, 0.75 and 0.82 were produced and labeled according: Zn40, Zn50, Zn60, Zn68, Zn75 and Zn82, respectively. After the synthesis, the nanoparticles were precipitated by adding 8 times in volume of a solution containing ethanol and acetone (4:1) followed by centrifugation (14000 rpm during 30 minutes). Finally, the oleic-acid coated hydrophobic samples in powder form were dispersed in chloroform or toluene.

2.3 Particle Induced X-Ray Emission (PIXE): The overall chemical composition of the samples was determined by PIXE measurements. They were performed with a 3 MeV H+ beam in a NEC 5SDH 1.7 MV tandem accelerator with a NEC RC43 end-station for material analysis. In this experiment the samples, in powder form, were attached to the sample holder using carbon tape. To obtain the final results, PIXE spectra were processed using GUPIX software.

2.4 Transmission Electron Microscopy (TEM): TEM and HRTEM images are obtained in a Philips CM200 transmission electron microscope equipped with an Ultra-Twin lens operating at 200 kV and by a FEI-Tecnai F30 at 300 kV Field Emission Gun (FEG) fitted with a SuperTwin® lens allowing a point resolution of 1.9 Å. TEM samples were prepared by dropping a chloroform solution containing the nanoparticles on a copper grid with an ultrathin hollow carbon film. The diameter (D) of each particle was obtained by measuring the area of transmission image and calculating a diameter supposing a circle. Then, the diameter distribution of each sample was obtained measuring about 500 particles. The mean diameter $<D>$ and size dispersion σ were obtained by fitting the size distribution with a lognormal distribution.

2.5 Magnetic measurements: Magnetization measurements as function of temperature in Field-Cooling and in Zero-Field-Cooling modes ($M_{FC}(T)$ and $M_{ZFC}(T)$, respectively, with using a field of 50 Oe, as well as function of applied field, were performed in a SQUID magnetometer (MPMS 5000 from Quantum Design). For this, the particles in toluene solution were mixed with epoxy resin and waited until completely solvent evaporation before the resin curing. The particle concentration in epoxy resin were about 0.2 wt% after subtraction the organic mass fraction estimated by the powder thermogravimetric measurements. AC magnetic measurements were carried out by means of Quantum Design PPMS P500 AC/DC Magnetometry System (ACMS) based on the mutual-inductance technique connected to a PPMS electronics system. The real (in-phase') and imaginary (out-of-phase χ") components of the AC magnetic susceptibility were measured as a function of temperature. Real and imaginary parts were measured with high accuracy by using a calibration coil array. Susceptibility was measured in the temperature range T = 100-350 K, varying the frequency in the 10 Hz to 10 kHz range with a driving field H = 14 Oe.

2.6 Hydrophilic MNPs: For magnetic fluid hyperthermia experiments performed in water and DMEM, the hydrophobic character of the as-made nanoparticles (oleic acid-coated) is changed to hydrophilic one. For this, the NPs are washed with methanol during 6 hours and subsequently in hot acetone (313 K) during 40 hours. After that, MNPs were precipitated by using a magnet and 10 mg of these washed NPs are added to 1.5 mL of 27% Ammonium Hydroxide solution (pH 11) containing anhydrous glucose (1000 mg). The NPs remain in this solution at 313 K during 20 hours, exposed to ultrasound for some intervals. Finally the nanoparticles were washed with water and diluted in a concentration of 0.1 wt% in water or DMEM.

2.7 Magnetic fluid hyperthermia (MFH): MFH experiments were performed in D5-F1 rf generator (nB – NanoScale Biomagnetics, Spain). The AC applied field has amplitude of H_0 = 200 Oe and frequency of f = 571 kHz. Initial temperature was the room temperature (about 292-294 K). To perform the MFH the particle in chloroform were dispersed in butter oil by intense sonication at 60 °C until the completely chloroform evaporation, while for the MFH experiments performed in water and DMEM, the hydrophilic ones are used. MNPs concentration of about 0.1 wt% in all matrixes were produced and confirmed by magnetic moment measurements. For this, the saturation magnetization of each nanoparticle was measured by using about 10 mg of powder. The amount of organic surfactants and solvent residues in each sample was taken into account from TGA measurements. After that, the concentration of the nanoparticles in the samples used in the

hyperthermia experiments was calculated by comparing the saturation magnetization with the respective magnetization curve. The main factor of error in the SLP determination are the numerical analyzes of the experimental data and the power loss due to no-adiabatic condition of the hyperthermia experiment. In order to reduce these effects, a double-wall vessel with a vacuum zone between them was used. Moreover, the power loss is proportional to the difference between the room temperature and the sample temperature (ΔT), with an exponential dependence with the time [39,40]. In this way, the sample was thermalized in the hyperthermia equipment for several minutes before to apply the magnetic field, and then the experiment was conducted until an increment of temperature (ΔT) not higher than 4 K is reached. Finally, the slope of $\Delta T/t$ used to calculate the SLP was obtained from the linear fit in the region of $\Delta T < 1$ K for all samples.

3. Results and Discussion

Representatives image of TEM in Bright Field Mode and sizes histograms of the Fe_3O_4 core and $Fe_3O_4/Zn_xCo_{1-x}Fe_2O_4$ core/shell samples are presented in the Fig. 1 and in Fig. S1 and S2 of the Supplementary material. A different morphology is observed when comparing the images of core with core/shell samples. Although the lattice parameters, density and atomic weight of the Fe_3O_4 and $Zn_xCo_{1-x}Fe_2O_4$ spinel phases are very similar, the shell overgrown polycrystalline, as observed from high resolution TEM (HRTEM) images of Zn50 nanoparticles shown in Fig. 1 and Fig. S1. The different crystal structure between Fe_3O_4 and $Zn_xCo_{1-x}Fe_2O_4$ ferrites NPs can be better analyzed by Fast Fourier Transform (FFT). Different interplanar distances of both compounds generate a mismatch strain at the interface that can be seen by inverse FFT, selecting suitable diffraction poles as is showed in the Fig. 1 (g), (h) and (i). In this example, the inverse FFT is taken of (022) and (113) diffraction planes which generates an image with information of these planes in the real space, reducing the background and eliminating the non selected crystalline planes. The procedure reveals a shell with similar crystalline orientation to the core but with a crystalline disorder layer at the interface due to the mismatch between different ferrites. From the size histogram fitting with a lognormal distribution, a mean core diameter $<D_{Core}>$ = 8.5 nm and standard deviation of $\sigma_{core} = 0.2$ is obtained. After the shell overgrowth, the total size of particles increases, as summarized in the Table 1. The average core/shell nanoparticles diameter grows up to 10.7 nm, indicating a shell thickness of 1.1 nm.

The analysis of the overall composition of the nanoparticles was performed by PIXE technique and the results are shown in Table 1. The measured atomic ratio between Zn and Co is lower than the nominal, but present a systematic evolution with it, changing from $\left[\frac{Zn}{Co+Zn}\right] = 0.33$ to $\left[\frac{Zn}{Co+Zn}\right] = 0.68$, for Zn40 and Zn80 MNPs systems, respectively. From this data, and assuming a stoichiometric Fe_3O_4 core with mean size of 8.5 nm and the mean total size of the core/shell particles, we calculated the shell stoichiometry shown in the Table 1.
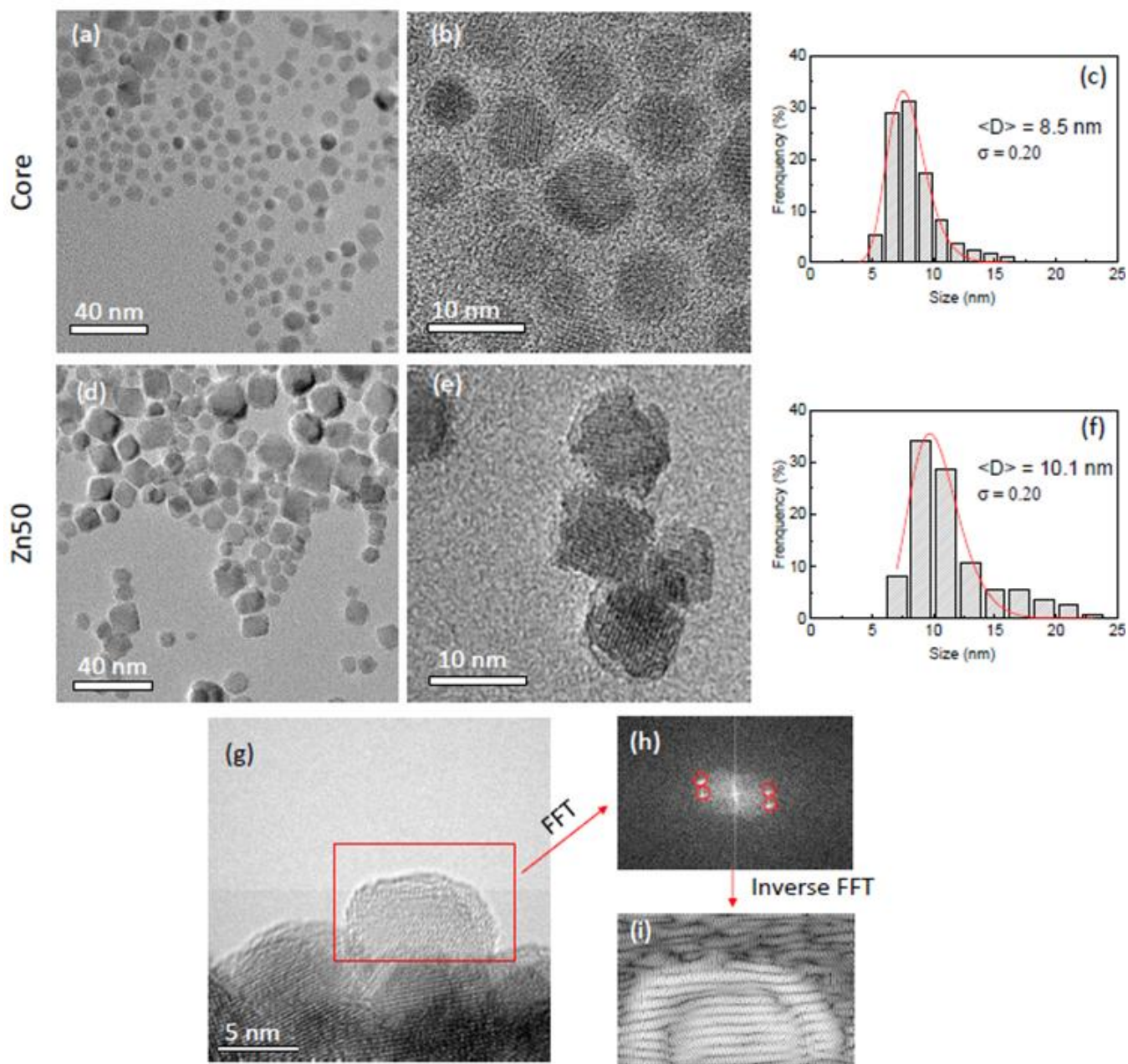
Figure 1. (a) and (b) TEM images of the core nanoparticles and (d) and (e) of the core/shell Zn50 sample. (c) and (f) are the size histograms of the core and Zn50, respectively. In (g) is presented HRTEM image where a FFT is performed of the red rectangle zone (h) followed by an inverse FFT with the red circle marks (i).

Table 1. Average particle size $<D>$ and distribution width σ from the fit of a lognormal size distribution of the TEM data. Chemical composition obtained by PIXE for the core and the $Fe_3O_4/Zn_xCo_{1-x}Fe_2O_4$ core/shell the samples. The shell stoichiometry was calculated assuming the $<D>$ values, and Fe_3O_4 cores of $<D>$=8.5 nm for all samples. The last

column shows the magnetic activation volume V_{mag} obtained from relaxation magnetization measurements.

Sample	TEM		PIXE			$\frac{Zn}{Co+Zn}$ (at%)	Calculated shell Stoichiometry	V_{mag} (nm)
	<D> (nm)	σ	Fe (%)	Co (%)	Zn (%)			
Core	8.5	0.20	-	-	-	-	-	9
Zn40	10.4	0.17	90.02(48)	6.69(24)	3.28(24)	33(5)	$Zn_{0.19}Co_{0.39}Fe_{2.41}O_4$	10.5
Zn50	10.9	0.19	89.99(56)	5.96(27)	4.05(30)	40(8)	$Zn_{0.21}Co_{0.31}Fe_{2.48}O_4$	10.4
Zn60	10.5	0.17	88.76(39)	5.55(19)	5.74(27)	51(8)	$Zn_{0.33}Co_{0.31}Fe_{2.36}O_4$	11.4
Zn68	10.7	0.14	90.10(41)	4.19(19)	5.71(29)	58(9)	$Zn_{0.31}Co_{0.23}Fe_{2.46}O_4$	12.0
Zn75	10.9	0.19	92.54(50)	2.92(21)	4.53(29)	61(11)	$Zn_{0.24}Co_{0.16}Fe_{2.60}O_4$	13.0
Zn82	11.0	0.20	90.66(40)	2.97(16)	6.37(27)	68(10)	$Zn_{0.33}Co_{0.15}Fe_{2.52}O_4$	10.3

Magnetization loops measured at 5 K are presented in Fig. 2. From these measurements it is noteworthy that the coercive field (H_C) of the core/shell samples decreases monotonously with the nominal zinc fraction in the shell, as shown in the inset of the figure and summarized in Table 2. This result indicates a decrease of the effective magnetic anisotropy K_{eff} of the core/shell samples with the Zn fraction, as was already found in similar nanomaterials.[32,33] The magnetization inversion process of $Fe_3O_4/Zn_xCo_{1-x}Fe_2O_4$ core/shell nanoparticles can be analyzed from the theoretical approach developed for bi-magnetic soft/hard exchange-coupled nanostructures, assuming a rigid magnetic coupling at the interface between the core and the shell; within this approximation the coercive field results: [30,31,33,41–43]

$$H_C = 2\frac{K^c_{eff}\rho_C + K^{Sh}_{eff}\rho_{Sh}}{M^c_S\rho_C + M^{Sh}_S\rho_{Sh}} \qquad (3)$$

where M_S is the magnetization saturation of each phase (c = core and sh = shell), ρ is the volume fraction and K_{eff} is the effective magnetic anisotropy of the core (c) and shell (sh). According to this model the H_C can be estimated for a core/shell particles from the core parameters M_S = 90 emu/g, <D_{core}> = 8.5 nm, K^c_{eff} = 3×10^5 erg/cm^3,[28] and shell parameters as thickness of 1 nm, K^{sh}_{eff} = 6×10^6 erg/cm^3 or 5×10^4 erg/cm^3 for the $CoFe_2O_4$[44] and $ZnFe_2O_4$[45] phases, respectively; resulting in H_C = 6.4 kOe and H_C = 0.4 kOe, respectively. These estimated values are in good agreement with the values experimentally obtained, supporting the rigid coupling between the core and shell where the effective magnetic anisotropy decreases with the Zn concentration of the shell.

Table 2. Parameters obtained from the magnetic measurements. The mean blocking temperature ($\langle T_B \rangle$) was obtained from the arithmetic mean of the distribution as $\langle T_B \rangle = \int T\, P(T)\, dT$, and distribution width (σ_{T_B}) was defined as variance, given by, $\sigma_{T_B}{}^2 = \int (\langle T_B \rangle - T)^2 P(T)\, dT$, where $P(T_B) = \frac{f(T_B)}{\int f(T)\, dT}$ is the probability density.

Sample	H_C (5K)	M_S	T_B		K_{eff}
			$\langle T_B \rangle$	σ_{T_B}	
	kOe	emu/g	K	K	x10^5 erg/cm^3
Core	0.4(0.1)	80(4)	28.5	29.5	3.0(1.7)
Zn40	5.4(0.4)	97(4)	164.8	75.2	10.9(2.5)
Zn50	4.4(0.3)	99(3)	127.1	62.0	8.7(3.0)
Zn60	3.7(0.3)	97(4)	153.5	73.5	8.3(2.6)
Zn68	3.3(0.3)	87(3)	130.3	57.9	5.8(2.4)
Zn75	2.0(0.2)	89(3)	106.8	62.2	3.7(3.0)
Zn82	1.8(0.2)	99(3)	99.3	52.9	6.9(2.5)

It can be noticed in Fig. 2 (see also Table 2) that the M_S of all samples does not change significantly, between 87-99 emu/g, when the shell stoichiometry changes, consistent with reported in previous works.[16,38]
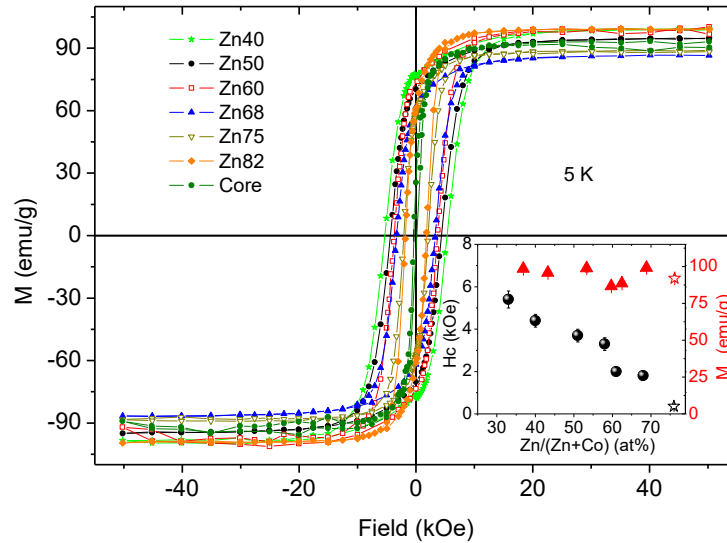

Figure 2. Hysteresis cycles of all samples measured at 5 K. In the inset the H_C (black dots) and M_S (red triangles) as function of the Zn/(Zn+Co) at% obtained by PIXE are shown. The H_C and M_S core values are also presented with empty stars.

At room temperature all the samples present reversible behavior when the magnetization loops are measured with DC field, as observed from Fig. S3, signaling that the nanoparticles systems are superparamagnetic at this temperature. In order to obtain the blocking temperature (T_B) of the systems, the magnetization curves were measured as function of temperature in Zero-field-cooling $M_{ZFC}(T)$ and field-cooling $M_{FC}(T)$ protocols, and on samples with 0.2 wt% dispersed in epoxy resin, as shown in Figure 3. For all core/shell samples, the maxima of $M_{ZFC}(T)$ curves (and the irreversible point) are located at higher temperatures than the corresponding nude magnetic core, indicating higher blocking temperatures associated to the $Zn_xCo_{1-x}Fe_2O_4$ shell. Figure 3 also shows the distribution of blocking temperature ($f(T_B)$) calculated from the magnetization curves for an assembly of non-interacting (or weakly interacting particles) as [46–49]:

$$f(T_B) \propto \frac{1}{T} \frac{d(M_{ZFC}(T) - M_{FC}(T))}{dT} \qquad (4)$$
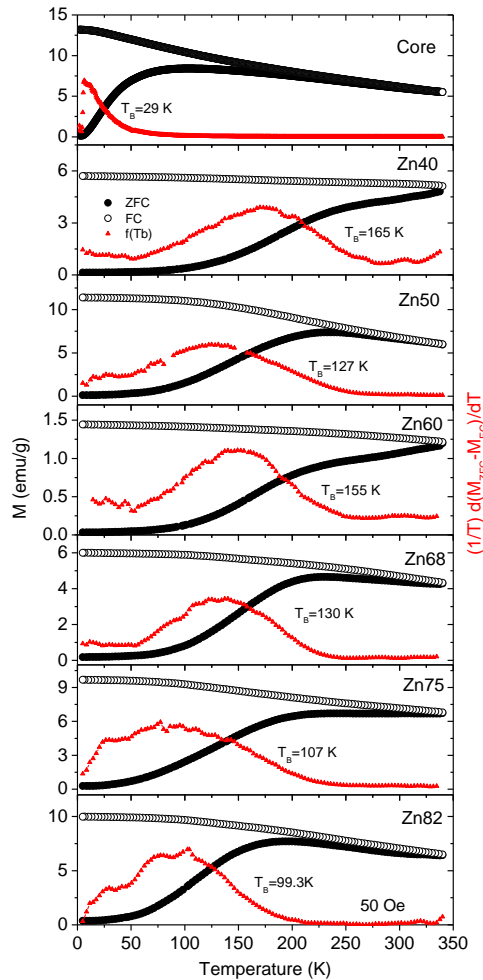

Figure 3. Temperature dependence of the $M_{ZFC}(T)$ and $M_{FC}(T)$ curves of the core and $Fe_3O_4/Zn_xCo_{1-x}Fe_2O_4$ NPs with 0.2 wt% in Epoxy resin and measured under applied field of 50 Oe. The red triangles is the distributions of blocked temperature $f(T_B)$ for each sample calculated from Equation 4.
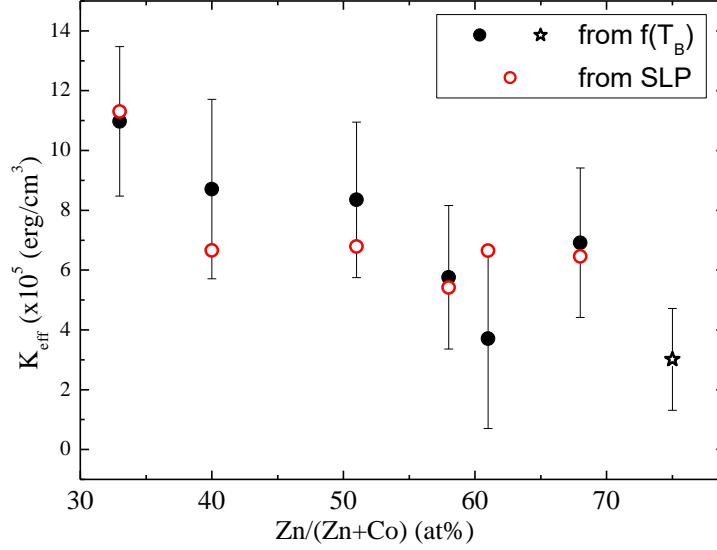
Figure 4. Magnetic anisotropy estimated from $<T_B>$, V_{mag}, and $\tau_0 = 2(1)\ 10^{-11}$ s experimental parameters, (solid black dots) and calculated from the SLP measurements (open red dot) as function of Zn/(Zn+Co) atomic shell ratio. The magnetic anisotropy of the core, estimated from $<T_B>$, is also presented with empty star.

The mean blocking temperature ($<T_B>$) is shown in Table 2 for all samples. It can be noticed that $<T_B>$ decreases as the Zn fraction increases, indicating a reduction of the energy barrier for the magnetic moment thermal fluctuation. In a system of non-interacting particles with uniaxial anisotropy, the energy barrier is defined as $K_{eff}V_{mag}$ and the corresponding blocking temperature is:

$$< T_B > = \frac{1}{k_B} ln\left(\frac{\tau_0}{\tau_m}\right) K_{eff} V_{mag} \qquad (5)$$

where V_{mag} is the magnetic volume, and τ_m is the measurement time (e.g. $\tau_m \sim 100$ s for DC magnetometry measurement and $\tau_m \sim 1/f$ for AC magnetometry and hyperthermia experiment). To extract reliable values of K_{eff} from the above relation, we performed further relaxation magnetization and ac-susceptibility measurements experiments to accurately determine V_{mag} and τ_0 of the present core/shell MNPs systems.

The magnetic volume was determined from the dependence of magnetic viscosity with respect to an external field at low temperature (T = 5 K). In a typical experiment, the sample is brought to a negative saturation field; then a reverse field is applied and the time dependence of magnetization is measured. This experiment is repeated for several reverse fields, around the coercivity value, in order to determine the maximum value of magnetic viscosity (S_{max}), as shown in Fig. S4. From S_{max} it is possible to obtain the so-called fluctuation field, H_f, which represents an effective field with the same effect on magnetization than thermal fluctuations.[50] With these parameters the magnetic activation volume obtained from $V_{mag} = k_BT/M_sH_f$ represents the smallest volume of material that reverses coherently in an event. [50,51] The values of V_{mag} for all samples are reported in Table 1. Details about the calculation of V_{mag} are provided in Supplementary Material. Remarkably, the obtained values of V_{mag} are in excellent agreement with the nanoparticle

10

volume measured by TEM (Table 1), as expected if the core and shell magnetic phases were rigidly coupled and therefore the magnetic moment undergo a coherent reversion against the energy barriers of the system.[50,52,53]

For all the samples the temperature dependence of χ'' shows a broad maximum that shift toward lower temperature when the frequency decreases. On the other hand, χ' presents a monotonous raising behavior in almost all samples except for the system with largest Zn concentration, Zn82, where also a frequency dependent peak is noticed (Fig. S5 Supplemental Material). For this sample, the frequency dependence of the χ'' peaks is successfully fitted with the phenomenological Vogel-Fulcher law as shown in Fig. S5,[54] resulted in $\tau_0 = 2(1)\ 10^{-11}$ s. When the Zn concentration decreases, the fitting of the frequency dependence peaks gives non-physical values of τ_0, in the 10^{-5}- 10^{-7}s range. This indicates that these exchange coupled core/shell systems with larger magnetic anisotropy are outside of the applicability of the model.

From the experimental parameters $<T_B>$, V_{mag}, and using $\tau_0 = 2(1)\ 10^{-11}$ s, obtained from the ZFC and FC magnetization, relaxation and ac-susceptibility measurements, respectively we have calculated the effective magnetic anisotropy for all the samples. The results are reported in Table 2 and in Fig. 4. As noticed, the K_{eff} decreases when the concentration of Zn increases.

Figure 5 shows the results of MFH experiments of the as-made hydrophobic nanoparticles (oleic acid-coated) with concentration of 0.1 wt% dispersed in butter oil ($\eta = 477$ mPas [55]), and 0.1 wt% hydrophilic nanoparticles (coated with glucose) dispersed in water ($\eta = 0.89$ mPas[56]) and DMEM ($\eta = 0.94$ mPas [57]). The measurements were performed with a field amplitude (H_0) of 200 Oe and a frequency of 571 kHz. The figure shows the variation of the temperature ΔT with time, with respect to the initial room temperature ~292-294 K. The specific loss power for all samples was estimated from the slope of the initial part of the $\Delta T(t)$ curve by:

$$SLP = (C_{liq}m_{liq}/m_{NPs})dT/dt \qquad\qquad (7)$$

where C_{liq} are the specific heat ($C_{butter\ oil} = 2.2$ J K^{-1} g^{-1}, $C_{water} = 4.18$ J K^{-1} g^{-1} and $C_{DMEM} = 4.18$ J K^{-1} g^{-1}), m_{liq} the mass of the liquid and m_{NPs} is the mass of the nanoparticles. The values of SLP for each sample dispersed in butter oil, water and DMEM were estimated from the initial slope of the evolution of temperature with time and presented on the right of Fig. 5. From these results it is observed that the samples have comparable heat absorption efficiencies, despite changes of viscosity by more than two orders of magnitude and the different hydrodynamic volumes. The independence of the SLP with the viscosity medium and the MNPs hydrodynamic volume indicates that the contribution of Brown mechanism in the heat generation is negligible and the Néel relaxation dominates. Conversely, when the SLP of different MNPs systems dispersed in the same medium are compared, a non-monotonous behavior of the SLP with the composition is observed with a clear maximum in the studied Zn composition range. When the MNPs are diluted in Butter oil the SLP maximum is observed for the sample with 50% of Zn/Zn+Co shell atomic ratio, and near 60 % when the samples are dispersed in water and DMEM. These results evidence that, by changing the effective anisotropy with the shell composition, the τ_N can be tuned to maximize the SLP value.
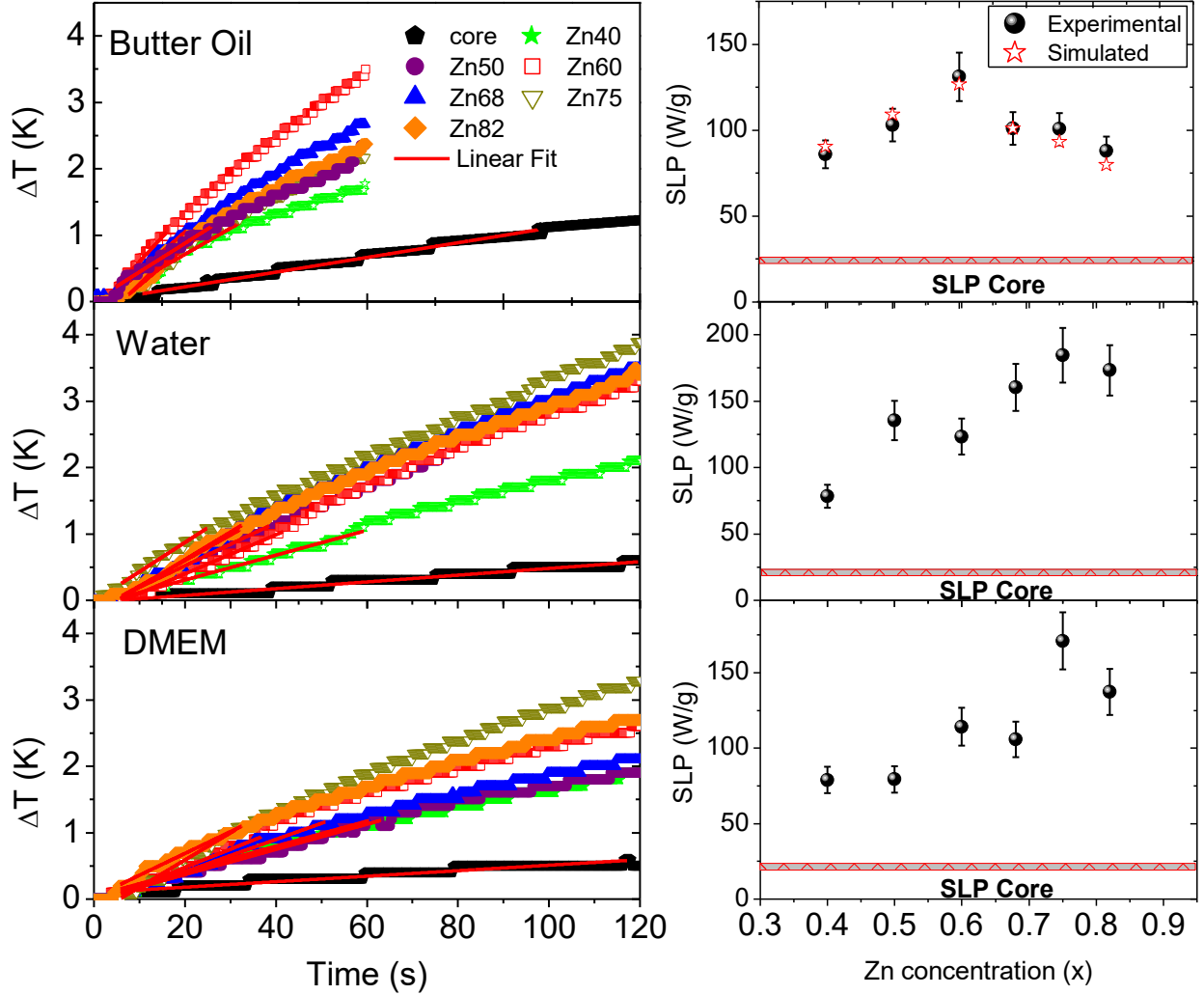
Figure 5. Panels on the left present the magnetic fluid hyperthermia experiments measured at 571 kHz and 200 Oe for the nanoparticles systems 0.1 wt% dispersed in butter oil (up), water (middle) and DMEM (down). Panels on the right give the SLP values as function of the measured Zn/(Zn+Co) atomic shell ratio, in butter oil (up), water (middle) and DMEM (down). The stars symbols display the simulated values of SLP for the core-shell nanoparticles dispersed in Butter-oil and the red lines are the SLP of Fe_3O_4 core nanoparticles.

In order to confirm this picture, the SLP were numerically calculated considering that only the magnetic mechanism corresponding to the Néel relaxation contributes to the heat absorption. The simulations were carried out using a model based on non-interacting single domain nanoparticles, as reported by De Biasi et al.[58] This model assumes that the nanoparticles are spatially fixed (i.e. the Brown's relaxation mechanism is not enabled) and the thermal effects are manifested in two different ways. The first effect is to promote the change of the magnetic moment orientation of the particles from an energy minimum to another, which is weighted by means of the probability to find a given particle in the superparamagnetic regime: $L \equiv L(H, T, \tau_m) = e^{-\tau_m/\tau^*}$, where τ^* is the effective inversion

time of the magnetization. This probability is the same used in Kinetic Monte Carlo calculations. [59–61] The second effect is the fluctuation of the magnetic moment within the same energy minimum, which results in the decrease of the effective magnetic moment, resulting in a statistical average of the magnetization vector projection in the direction of the applied field ($\langle\vec{\mu}\rangle$). Taking these considerations in to account, the total average magnetization of the system as a function of time is given by:

$$\langle\vec{M}\rangle = \langle\vec{\mu}\rangle_{SP}\, L + (1-L)[P_0\,\langle\vec{\mu}\rangle_0 + P_1\,\langle\vec{\mu}\rangle_1] \qquad (8)$$

where $\langle\vec{\mu}\rangle_{SP}\, L$ corresponds to the superparamagnetic contribution and $(1-L)[P_0\,\langle\vec{\mu}\rangle_0 + P1\,\mu1$ to the blocked one. The subscript *SP* indicates the integration region corresponding to the entire phase space, while the subscripts *0* and *1* indicate the respective energy minimum associated to the energy landscape determined by external field that corresponds to the integration interval, with respective normalized population given by P_0 and P_1 ($P_0+P_1=1$). The temporal evolution of magnetization is reflected in two aspects: firstly, the variation of the energy landscape, which results in changes of the statistical averages; secondly, the evolution of the populations P_0 and P_1 due to the inversion in the magnetization of some particles of the assembly given by $P_0(t+\delta t) = P_0(t)+L[P_0^\infty-P_0(t)]$, where δt is the time interval within which the problem has been discretized ($\delta H/\delta t$ is the sweep speed of the external field) and P_0^∞ is the equilibrium population associated with the minimum energy *0*. To perform the calculation the experimental data were taken as input of the magnetic relaxation (See Tables 1 and 2), namely the magnetic saturation M_S, the magnetic activation volume, τ_0, and the frequency of the hyperthermia experiment ($f = 571$ kHz), and the applied field parameters ($H_0 = 200$ Oe). We assumed that the easy axes of the particles are randomly oriented. The simulated SLP data are shown in Fig. 5 for the highest viscosity medium, which are in good agreement with the values obtained from the experimental curve. In the simulations we have allowed to vary only the value of the effective anisotropy energy density K_{eff}, forcing the rest of the parameters to be fixed, according to the experimental conditions. In Fig. 4 we compare the obtained density of magnetic anisotropy energy from the simulations with the experimental values, where a very good agreement is obtained. These results also confirm that the Néel magnetic relaxation is the dominant mechanism.

Notice that although the shell grows epitaxial over the core, a disordered interface was resolved and also multigrain shell structure was observed. However, dc-magnetic measurements are consistent with rigid magnetic coupling between the core and shell phases where single phase coercive loops were observed for all the temperature and composition range. This picture is strongly supported by the magnetic relaxation measurements where the activation volume, which corresponds to the smallest volume that reverses coherently in an event, coincides with the measured by TEM. Within the rigid coupling regime the magnetic anisotropy can be extrapolated from the properties of the core and shell phases which facilitate the design of core/shell system. In fact, the measured coercive fields for the $Fe_3O_4/Zn_xCo_{1-x}Fe_2O_4$ systems agree with the average coercivity expected for a powder of rigid coupled hard/soft magnetic nanoparticles. The measurements also evidence the presence of weak magnetic interactions, ascribed to dipolar interparticle interaction that cannot be neglected despite the large nanoparticles dispersions (0.2 wt% for the magnetic measurements).

The magnetic hyperthermia experiment with the nanoparticles dispersed in different mediums shows very similar values of specific loss power, even when the viscosity of the mediums is more than two orders of magnitude different. This result confirms that the Néel relaxation is the dominant mechanism, which is the expected one for butter oil due to its large viscosity that inhibits the physical movement of the nanoparticles in the MFH condition. Notice that if the particles have a coherent inversion of the magnetic moment, and the magnetization response is linear with the alternating magnetic field, the Rosensweig's model predicts the optimum SLP when the characteristic time of the experiment are in correspondence with the relaxation time of the system as: $2\pi f\tau = 1$. [5] In the present MNPs system the coherent inversion of the magnetic moment is supported by the rigid core/shell coupling, and the agreement between the magnetic activation volume and the volume measured by TEM. Moreover as the hyperthermia experiments were performed with larger nanoparticles dispersion the system approaches to the hypothesis of non-interacting nanoparticles. Therefore, because the Brown mechanism is avoided for these systems, the Néel relaxation time can be adjusted by a fine tuning of the effective energy barrier until it reaches the optimum value for the frequency used in the MFH experiments. Notice that to do a fine tuning of the Néel relaxation time, the size of the nanoparticles is not a proper parameter since small variations of it results in large changes of the energy barrier. Instead, the core/shell NPs shown to be ideal systems since they can be designed with comparable size and magnetization and they allow the fine adjustment of the magnetic anisotropy by adjusting the composition of a thin magnetic shell. For the core/shell MNPs studied in this work, the optimum conditions were observed near of 50 % of Zn/(Zn+Co) atomic shell ratio, when the MNPs are dispersed in butter oil, whereas the same MNPs displayed optimum heating near 60 % when they are dispersed in water and DMEM. The experimentally SLP observed values were successfully described by a simple model considering non-interacting magnetic moments where the Néel relaxation is the only active mechanism to produce magnetic losses, with the effective magnetic anisotropy as the single adjusted parameter. The obtained value of the magnetic anisotropy from the SLP fitting was in excellent agreement with that calculated from dc-magnetization, showing a systematic decreasing when the Zn concentration increases. These strongly coupled core/shell MNPs provide a successful method to produce highly efficient heaters for viscous media such as the intracellular medium, through the control of the shell composition. This method could be in principle applied to MNPs of different sizes to improve their heat efficiency, which is a key requisite for many MFH-based therapeutic applications.

4. Conclusions

The strategy to tune the effective magnetic anisotropy of MNPs presented in this work, is based on controlling the phase composition of magnetically coupled core/shell nanoparticles. This allows to find the optimal composition, for a given particle size, that maximizes the heating efficiency of the system, even in highly viscous media. We showed that by changing the shell composition of ~10.7 nm $Fe_3O_4/Zn_xCo_{1-x}Fe_2O_4$ core/shell nanoparticles, the effective magnetic anisotropy can be changed from 11×10^5 erg/cm^3 to 4×10^5 erg/cm^3 when the Zn atomic ratio (Zn/(Zn+Co)) increases. In this way, proper

condition to optimize the specific loss power in magnetic fluid hyperthermia can be tuned for each working frequency. Thereby, the modulation of the composition of the thin shell coating and the interface core/shell nanoparticle coupling permits not only the optimization of the heating power, maintaining the overall nanoparticle size and magnetization value, but it also improves the reproducibility of magnetic nanoparticles heating properties when they are dispersed in media of different viscosity. Moreover, by combining in a single nanoparticle a soft magnetic core with a hard magnetic shell, the magnetic anisotropy can be enhanced, which allows to reach the optimum heating condition for lower nanoparticles size. Our results open new possibilities to overcome current limitations in clinical MFH, optimizing the heating power and extending the workability of the magnetic fluid hyperthermia to applications that require nanoparticles of smaller sizes.

References

[1]   K. Mahmoudi, A. Bouras, D. Bozec, R. Ivkov, C. Hadjipanayis, Magnetic hyperthermia therapy for the treatment of glioblastoma: a review of the therapy's history, efficacy and application in humans, Int. J. Hyperth. 34 (2018) 1316–1328. https://doi.org/10.1080/02656736.2018.1430867.

[2]   K. Maier-Hauff, F. Ulrich, D. Nestler, H. Niehoff, P. Wust, B. Thiesen, H. Orawa, V. Budach, A. Jordan, Efficacy and safety of intratumoral thermotherapy using magnetic iron-oxide nanoparticles combined with external beam radiotherapy on patients with recurrent glioblastoma multiforme, J. Neurooncol. 103 (2011) 317–324. https://doi.org/10.1007/s11060-010-0389-0.

[3]   N.D. Thorat, J. Bauer, Functional smart hybrid nanostructures based nanotheranostic approach for advanced cancer treatment, Appl. Surf. Sci. 527 (2020) 146809. https://doi.org/10.1016/j.apsusc.2020.146809.

[4]   N.A. Usov, B.Y. Liubimov, Dynamics of magnetic nanoparticle in a viscous liquid: Application to magnetic nanoparticle hyperthermia, J. Appl. Phys. 112 (2012). https://doi.org/10.1063/1.4737126.

[5]   R.E. Rosensweig, Heating magnetic fluid with alternating magnetic field, J. Magn. Magn. Mater. 252 (2002) 370–374. https://doi.org/10.1016/S0304-8853(02)00706-0.

[6]   E. Lima, E. De Biasi, R.D. Zysler, M. Vasquez Mansilla, M.L. Mojica-Pisciotti, T.E. Torres, M.P. Calatayud, C. Marquina, M. Ricardo Ibarra, G.F. Goya, Relaxation time diagram for identifying heat generation mechanisms in magnetic fluid hyperthermia, J. Nanoparticle Res. 16 (2014) 1–11. https://doi.org/10.1007/s11051-014-2791-6.

[7]   E. Liu, Y. Yin, L. Sun, Y. Zhai, J. Du, F. Xu, H. Zhai, Increasing spin polarization in Fe_3O_4 films by engineering antiphase boundary densities, Appl. Phys. Lett. 110 (2017) 142402. https://doi.org/10.1063/1.4979586.

[8]   U.S. Patil, S. Adireddy, A. Jaiswal, S. Mandava, B.R. Lee, D.B. Chrisey, In vitro/in vivo toxicity evaluation and quantification of iron oxide nanoparticles, 2015. https://doi.org/10.3390/ijms161024417.

[9]   R. Hergt, S. Dutz, M. Röder, Effects of size distribution on hysteresis losses of magnetic nanoparticles for hyperthermia, J. Phys. Condens. Matter. 20 (2008) 385214. https://doi.org/10.1088/0953-8984/20/38/385214.

[10] M. Gonzales-Weimuller, M. Zeisberger, K.M. Krishnan, Size-dependant heating rates of iron oxide nanoparticles for magnetic fluid hyperthermia, J. Magn. Magn. Mater. 321 (2009) 1947–1950. https://doi.org/10.1016/j.jmmm.2008.12.017.

[11] M.M. Cruz, L.P. Ferreira, J. Ramos, S.G. Mendo, A.F. Alves, M. Godinho, M.D. Carvalho, Enhanced magnetic hyperthermia of CoFe2O4and MnFe2O4nanoparticles, J. Alloys Compd. 703 (2017) 370–380. https://doi.org/10.1016/j.jallcom.2017.01.297.

[12] S.H. Noh, W. Na, J.T. Jang, J.H. Lee, E.J. Lee, S.H. Moon, Y. Lim, J.S. Shin, J. Cheon, Nanoscale magnetism control via surface and exchange anisotropy for optimized ferrimagnetic hysteresis, Nano Lett. 12 (2012) 3716–3721. https://doi.org/10.1021/nl301499u.

[13] R. Di Corato, A. Espinosa, L. Lartigue, M. Tharaud, S. Chat, T. Pellegrino, C. Ménager, F. Gazeau, C. Wilhelm, Magnetic hyperthermia efficiency in the cellular environment fordifferent nanoparticle designs, Biomaterials. 35 (2014) 6400–6411. https://doi.org/10.1016/j.biomaterials.2014.04.036.

[14] S. He, H. Zhang, Y. Liu, F. Sun, X. Yu, X. Li, L. Zhang, L. Wang, K. Mao, G. Wang, Y. Lin, Z. Han, R. Sabirianov, H. Zeng, Maximizing Specific Loss Power for Magnetic Hyperthermia by Hard–Soft Mixed Ferrites, Small. 14 (2018) 1–9. https://doi.org/10.1002/smll.201800135.

[15] R.D. Raland, D. Saikia, C. Borgohain, J.P. Borah, Heating efficiency and correlation between the structural and magnetic properties of oleic acid coated MnFe2O4 nanoparticles for magnetic hyperthermia application, J. Phys. D. Appl. Phys. 50 (2017). https://doi.org/10.1088/1361-6463/aa77e9.

[16] G.C. Lavorato, R. Das, Y. Xing, J. Robles, F.J. Litterst, E. Baggio-Saitovich, M.H. Phan, H. Srikanth, Origin and Shell-Driven Optimization of the Heating Power in Core/Shell Bimagnetic Nanoparticles, ACS Appl. Nano Mater. 3 (2020) 1755–1765. https://doi.org/10.1021/acsanm.9b02449.

[17] K. Simeonidis, C. Martinez-Boubeta, D. Serantes, S. Ruta, O. Chubykalo-Fesenko, R. Chantrell, J. Oró-Solé, L. Balcells, A.S. Kamzin, R.A. Nazipov, A. Makridis, M. Angelakeris, Controlling Magnetization Reversal and Hyperthermia Efficiency in Core–Shell Iron–Iron Oxide Magnetic Nanoparticles by Tuning the Interphase Coupling, ACS Appl. Nano Mater. 3 (2020) 4465–4476. https://doi.org/10.1021/acsanm.0c00568.

[18] A. Gangwar, S. Kumar, S.S. Meena, A. Sharma, M.K. Viswanadh, K. Neogi, M.S. Muthu, N.K. Prasad, Structural and in-vitro assessment of ZnxFe3−xC ($0 \leq x \leq 1$) nanoparticles as magnetic biomaterials, Appl. Surf. Sci. 509 (2020) 144891. https://doi.org/10.1016/j.apsusc.2019.144891.

[19] A.H. Lu, E.L. Salabas, F. Schüth, Magnetic nanoparticles: Synthesis, protection, functionalization, and application, Angew. Chemie - Int. Ed. 46 (2007) 1222–1244. https://doi.org/10.1002/anie.200602866.

[20] A.Y. Zubarev, Magnetic hyperthermia in a system of immobilized magnetically interacting particles, Phys. Rev. E. 99 (2019) 1–6. https://doi.org/10.1103/PhysRevE.99.062609.

[21] R. Fu, Y. Yan, C. Roberts, Z. Liu, Y. Chen, The role of dipole interactions in hyperthermia heating colloidal clusters of densely-packed superparamagnetic nanoparticles, Sci. Rep. 8 (2018) 1–10. https://doi.org/10.1038/s41598-018-23225-5.

[22] D. Serantes, D. Baldomir, C. Martinez-Boubeta, K. Simeonidis, M. Angelakeris, E. Natividad, M. Castro, A. Mediano, D.X. Chen, A. Sanchez, L.I. Balcells, B. Martínez, Influence of dipolar interactions on hyperthermia properties of ferromagnetic particles, J. Appl. Phys. 108 (2010). https://doi.org/10.1063/1.3488881.

[23] E. Lima, E. De Biasi, M.V. Mansilla, M.E. Saleta, M. Granada, H.E. Troiani, F.B. Effenberger, L.M. Rossi, H.R. Rechenberg, R.D. Zysler, Heat generation in agglomerated ferrite nanoparticles in an alternating magnetic field, J. Phys. D. Appl. Phys. 46 (2013). https://doi.org/10.1088/0022-3727/46/4/045002.

[24] B. Sanz, M.P. Calatayud, E. De Biasi, E. Lima, M.V. Mansilla, R.D. Zysler, M.R. Ibarra, G.F. Goya, In silico before in vivo: How to predict the heating efficiency of magnetic nanoparticles within the intracellular space, Sci. Rep. 6 (2016). https://doi.org/10.1038/srep38733.

[25] D. Serantes, K. Simeonidis, M. Angelakeris, O. Chubykalo-Fesenko, M. Marciello, M. Del Puerto Morales, D. Baldomir, C. Martinez-Boubeta, Multiplying magnetic hyperthermia response by nanoparticle assembling, J. Phys. Chem. C. 118 (2014) 5927–5934. https://doi.org/10.1021/jp410717m.

[26] E.A. Périgo, G. Hemery, O. Sandre, D. Ortega, E. Garaio, F. Plazaola, F.J. Teran, Fundamentals and advances in magnetic hyperthermia, Appl. Phys. Rev. 2 (2015). https://doi.org/10.1063/1.4935688.

[27] G. Salas, J. Camarero, D. Cabrera, H. Takacs, M. Varela, R. Ludwig, H. Dähring, I. Hilger, R. Miranda, M.D.P. Morales, F.J. Teran, Modulation of magnetic heating via dipolar magnetic interactions in monodisperse and crystalline iron oxide nanoparticles, J. Phys. Chem. C. 118 (2014) 19985–19994. https://doi.org/10.1021/jp5041234.

[28] E. Lima, A.L. Brandl, A.D. Arelaro, G.F. Goya, Spin disorder and magnetic anisotropy in Fe3 O4 nanoparticles, J. Appl. Phys. 99 (2006). https://doi.org/10.1063/1.2191471.

[29] M. Vasilakaki, K.N. Trohidou, J. Nogués, Enhanced Magnetic Properties in Antiferromagnetic-Core/Ferrimagnetic-Shell Nanoparticles, Sci. Rep. 5 (2015) 9609. https://doi.org/10.1038/srep09609.

[30] R. Skomski, J.M.D. Coey, Giant energy product in nanostructured two-phase magnets, Phys. Rev. B. 48 (1993) 15812–15816. https://doi.org/10.1103/PhysRevB.48.15812.

[31] E.F. Kneller, R. Hawig, The exchange-spring magnet: a new material principle for permanent magnets, IEEE Trans. Magn. 27 (1991) 3588–3560. https://doi.org/10.1109/20.102931.

[32] E.L. Winkler, E. Lima, D. Tobia, M.E. Saleta, H.E. Troiani, E. Agostinelli, D. Fiorani, R.D. Zysler, Origin of magnetic anisotropy in ZnO/CoFe2O4 and CoO/CoFe2O4 core/shell nanoparticle systems, Appl. Phys. Lett. 101 (2012) 252405. https://doi.org/10.1063/1.4771993.

[33] G.P. Zhao, M.G. Zhao, H.S. Lim, Y.P. Feng, C.K. Ong, From nucleation to coercivity, Appl. Phys. Lett. 87 (2005) 1–3. https://doi.org/10.1063/1.2108120.

[34] E.E. Fullerton, J.. Jiang, S.. Bader, Hard/soft magnetic heterostructures: model exchange-spring magnets, J. Magn. Magn. Mater. 200 (1999) 392–404. https://doi.org/10.1016/S0304-8853(99)00376-5.

[35] G. Lavorato, E. Winkler, Thickness dependence of exchange coupling in epitaxial Fe 3 O 4 / CoFe 2 O 4 soft / hard magnetic bilayers, 054405 (2016) 1–6. https://doi.org/10.1103/PhysRevB.94.054405.

[36] U. Klekotka, B. Piotrowska, D. Satuła, B. Kalska-Szostko, Modified ferrite core-shell nanoparticles magneto-structural characterization, Appl. Surf. Sci. 444 (2018) 161–167. https://doi.org/10.1016/j.apsusc.2018.02.212.

[37] G.C. Lavorato, E. Lima, H.E. Troiani, R.D. Zysler, E.L. Winkler, Tuning the coercivity and exchange bias by controlling the interface coupling in bimagnetic core/shell nanoparticles, Nanoscale. 9 (2017) 10240–10247. https://doi.org/10.1039/C7NR03740F.

[38] F. Fabris, E. Lima, E. De Biasi, H.E. Troiani, M. Vásquez Mansilla, T.E. Torres, R. Fernández Pacheco, M.R. Ibarra, G.F. Goya, R.D. Zysler, E.L. Winkler, Controlling the dominant magnetic relaxation mechanisms for magnetic hyperthermia in bimagnetic core–shell nanoparticles, Nanoscale. 11 (2019) 3164–3172. https://doi.org/10.1039/C8NR07834C.

[39] A. Makridis, S. Curto, G.C. van Rhoon, T. Samaras, M. Angelakeris, A standardisation protocol for accurate evaluation of specific loss power in magnetic hyperthermia, J. Phys. D. Appl. Phys. 52 (2019) 255001. https://doi.org/10.1088/1361-6463/ab140c.

[40] R.R. Wildeboer, P. Southern, Q.A. Pankhurst, On the reliable measurement of specific absorption rates and intrinsic loss parameters in magnetic hyperthermia materials, J. Phys. D. Appl. Phys. 47 (2014) 495003. https://doi.org/10.1088/0022-3727/47/49/495003.

[41] G.P. Zhao, X.L. Wang, Nucleation, pinning, and coercivity in magnetic nanosystems: An analytical micromagnetic approach, Phys. Rev. B - Condens. Matter Mater. Phys. 74 (2006) 2–5. https://doi.org/10.1103/PhysRevB.74.012409.

[42] T. Leineweber, H. Kronmüller, Micromagnetic examination of exchange coupled ferromagnetic nanolayers, J. Magn. Magn. Mater. 176 (1997) 145–154. https://doi.org/10.1016/S0304-8853(97)00601-X.

[43] F. Fabris, E. Lima, C. Quinteros, L. Neñer, M. Granada, M. Sirena, R.D. Zysler, H.E. Troiani, V. Leborán, F. Rivadulla, E.L. Winkler, Tunnel Magnetoresistance in Self-Assemblies of Exchange-Coupled Core/Shell Nanoparticles, Phys. Rev. Appl. 11 (2019) 054089. https://doi.org/10.1103/PhysRevApplied.11.054089.

[44] F. Fabris, Y.T. Xing, D.F. Franceschini, D.R. Sanchez, M. Alzamora, W.C. Nunes, Effects of postdeposition heat treatment on the structural and magnetic properties of CoFe2O4 nanoparticles produced by pulsed laser deposition, J. Appl. Phys. 122 (2017). https://doi.org/10.1063/1.4985789.

[45] C. Yao, Q. Zeng, G.F. Goya, T. Torres, J. Liu, H. Wu, M. Ge, Y. Zeng, Y. Wang, J.Z. Jiang, ZnFe 2 O 4 Nanocrystals : Synthesis and Magnetic Properties, J. PHys. Chem. C. 111 (2007) 12274–12278. https://doi.org/10.1021/jp0732763.

[46] I.J. Bruvera, P. Mendoza Zélis, M. Pilar Calatayud, G.F. Goya, F.H. Sánchez, Determination of the blocking temperature of magnetic nanoparticles: The good, the bad, and the ugly, J. Appl. Phys. 118

(2015). https://doi.org/10.1063/1.4935484.

[47]   J.S. Micha, B. Dieny, J.R. Régnard, J.F. Jacquot, J. Sort, Estimation of the Co nanoparticles size by magnetic measurements in Co/SiO2 discontinuous multilayers, J. Magn. Magn. Mater. 272–276 (2004) 2003–2004. https://doi.org/10.1016/j.jmmm.2003.12.268.

[48]   K.L. Livesey, S. Ruta, N.R. Anderson, D. Baldomir, R.W. Chantrell, D. Serantes, Beyond the blocking model to fit nanoparticle ZFC/FC magnetisation curves, Sci. Rep. 8 (2018) 1–9. https://doi.org/10.1038/s41598-018-29501-8.

[49]   G.C. Lavorato, E. Lima Jr, D. Tobia, D. Fiorani, H.E. Troiani, R.D. Zysler, E.L. Winkler, Size effects in bimagnetic CoO/CoFe 2 O 4 core/shell nanoparticles, Nanotechnology. 25 (2014) 355704. https://doi.org/10.1088/0957-4484/25/35/355704.

[50]   D. Peddis, C. Cannas, G. Piccaluga, E. Agostinelli, D. Fiorani, Spin-glass-like freezing and enhanced magnetization in ultra-small CoFe2O4 nanoparticles, Nanotechnology. 21 (2010) 125705.

[51]   K.O. Grady, H. Laidler, The limits to magnetic recording * media considerations, 200 (1999) 616–633.

[52]   S. Laureti, G. Varvaro, a M. Testa, D. Fiorani, E. Agostinelli, G. Piccaluga, a Musinu, a Ardu, D. Peddis, Magnetic interactions in silica coated nanoporous assemblies of CoFe2O4 nanoparticles with cubic magnetic anisotropy., Nanotechnology. 21 (2010) 315701. https://doi.org/10.1088/0957-4484/21/31/315701.

[53]   G.C. Lavorato, E. Lima, H.E. Troiani, R.D. Zysler, E.L. Winkler, Exchange-coupling in thermal annealed bimagnetic core/shell nanoparticles, J. Alloys Compd. 633 (2015) 333–337. https://doi.org/10.1016/j.jallcom.2015.02.050.

[54]   G. Lavorato, E. Winkler, A. Ghirri, E. Lima, D. Peddis, H.E. Troiani, D. Fiorani, E. Agostinelli, D. Rinaldi, R.D. Zysler, Exchange bias and surface effects in bimagnetic CoO-core/Co0.5Ni0.5Fe2O4-shell nanoparticles, Phys. Rev. B. 94 (2016) 054432. https://doi.org/10.1103/PhysRevB.94.054432.

[55]   H. Hayashi, Viscoelasticity of Butter, Springer US, Boston, MA, 1994, 1994.

[56]   J.R. Rumble, CRC Handbook of Chemistry and Physics, 98th Editi, Boca Raton London New York CRC Press, Taylor & Francis Group [2017], 2017.

[57]   E. Fröhlich, G. Bonstingl, A. Höfler, C. Meindl, G. Leitinger, T.R. Pieber, E. Roblegg, Comparison of two in vitro systems to assess cellular effects of nanoparticles-containing aerosols., Toxicol. In Vitro. 27 (2013) 409–417. https://doi.org/10.1016/j.tiv.2012.08.008.

[58]   E. De Biasi, R.D. Zysler, C.A. Ramos, M. Knobel, A new model to describe the crossover from superparamagnetic to blocked magnetic nanoparticles, J. Magn. Magn. Mater. 320 (2008) 312–315. https://doi.org/10.1016/j.jmmm.2008.02.160.

[59]   M. Anand, V. Banerjee, J. Carrey, Relaxation in one-dimensional chains of interacting magnetic nanoparticles: Analytical formula and kinetic Monte Carlo simulations, Phys. Rev. B. 99 (2019) 1–11. https://doi.org/10.1103/PhysRevB.99.024402.

[60]   D. Niculaes, A. Lak, G.C. Anyfantis, S. Marras, O. Laslett, S.K. Avugadda, M. Cassani, D. Serantes, O. Hovorka, R. Chantrell, T. Pellegrino, Asymmetric Assembling of Iron Oxide Nanocubes for Improving Magnetic Hyperthermia Performance, ACS Nano. 11 (2017) 12121–12133. https://doi.org/10.1021/acsnano.7b05182.

[61]   R.P. Tan, J. Carrey, M. Respaud, Magnetic hyperthermia properties of nanoparticles inside lysosomes using kinetic Monte Carlo simulations: Influence of key parameters and dipolar interactions, and evidence for strong spatial variation of heating power, Phys. Rev. B - Condens. Matter Mater. Phys. 90 (2014) 1–12. https://doi.org/10.1103/PhysRevB.90.214421.

Supplementary material

Adjusting the Néel relaxation time of Fe_3O_4/$Zn_xCo_{1-x}Fe_2O_4$ core/shell nanoparticles for optimal heat generation in magnetic hyperthermia

Fernando Fabris, Javier Lohr, Enio Lima Jr., Adriele Aparecida de Almeida, Horacio E. Troiani, Luis M. Rodríguez, Marcelo Vásquez Mansilla, Myriam H. Aguirre, Gerardo F. Goya, Daniele Rinaldi, Alberto Ghirri, Davide Peddis, Dino Fiorani, Roberto D. Zysler, Emilio De Biasi and Elin L. Winkler
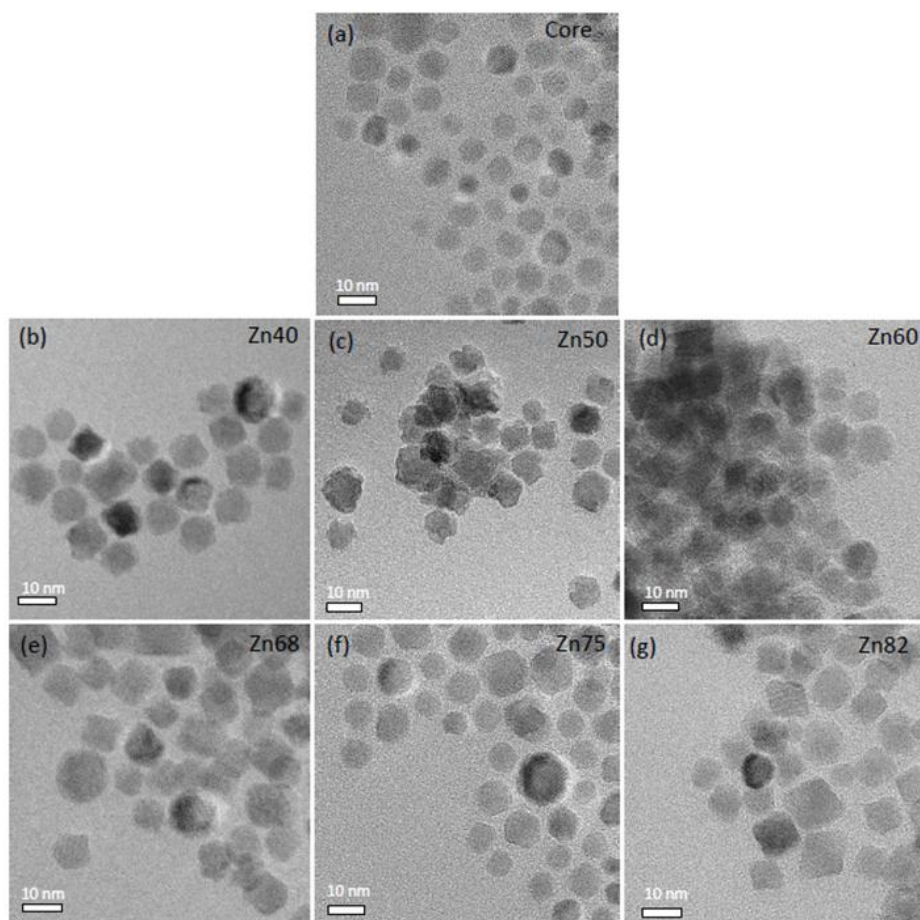
Figure S1. TEM images of the core (a) and core/shell samples: Zn40 (b), Zn50 (c), Zn60 (d), Zn68 (e), Zn75 (f), and Zn82 (g).

Figure S1 shows representative images of Fe_3O_4 core and the $Fe_3O_4/Zn_xCo_{1-x}Fe_2O_4$ core/shell nanoparticles. The corresponding size histograms are presented in Figure S2. From the size histogram fitted with a lognormal distribution, a mean core diameter $<D_{Core}>$ = 8.5 nm with standard deviation of σ_{core} = 0.2 is obtained. The average core/shell nanoparticles diameter grows up to ~10.7 nm, indicating a shell thickness of 1.1 nm. Figure S3 shows the DC magnetization loops at room temperature for Fe_3O_4 core and the $Fe_3O_4/Zn_xCo_{1-x}Fe_2O_4$ core/shell nanoparticles. Notice that all the samples present reversible behavior, signaling that the systems are superparamagnetic at this temperature.
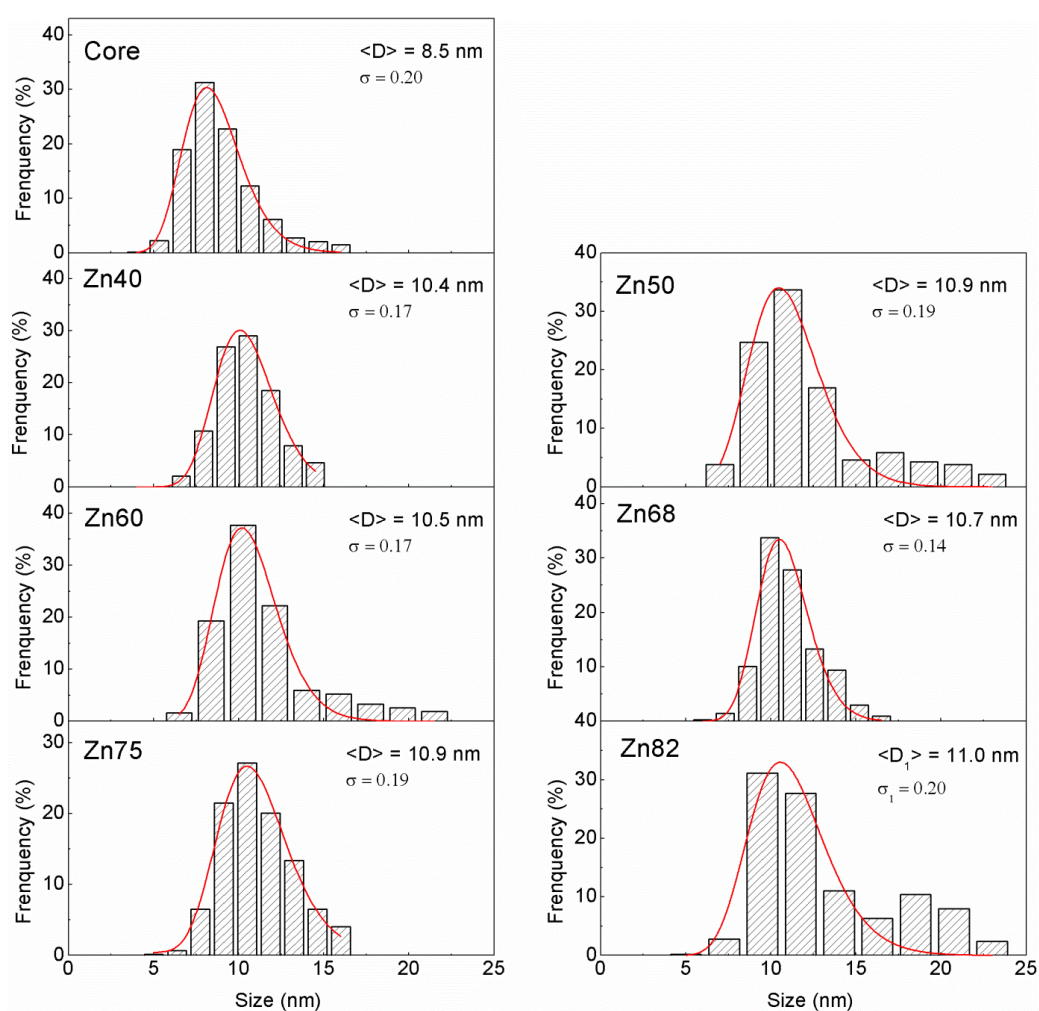

Figure S2. Size distribution to the Fe_3O_4 core and $Fe_3O_4/Zn_xCo_{1-x}Fe_2O_4$ core/shell samples fitted with a log-normal distribution (red line) to determine the mean diameter and the dispersion size which are presented in the Table 1.
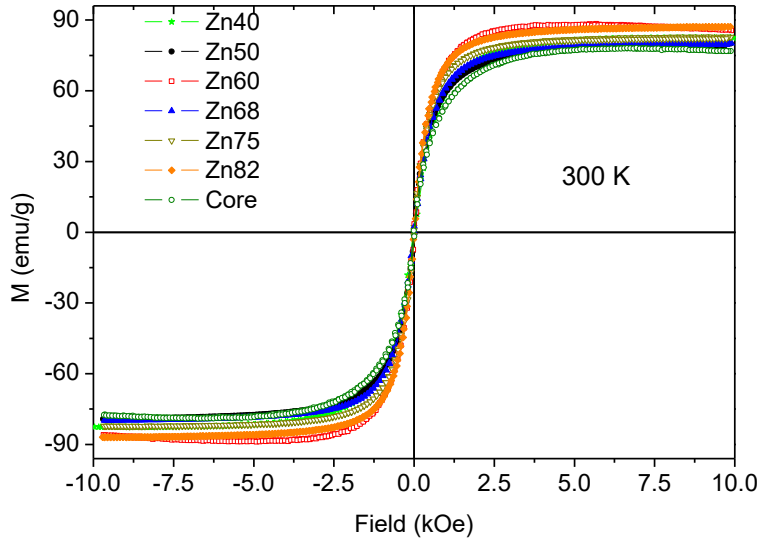
Figure S3. Magnetization loops of the Fe_3O_4 core and $Fe_3O_4/Zn_xCo_{1-x}Fe_2O_4$ core/shell nanoparticles measured at 300 K.

In order to determine the magnetic activation volume V_{mag} of the core/shell nanoparticles, the dependence of magnetic viscosity with respect to an external field at low temperature (5 K) has been investigated. In an ensemble of magnetic nanoparticles, the time relaxation of magnetization is characterized by a distribution of energy barriers (i.e. activation energies), and it is often found to be logarithmic:

$$M(t) = M(t_0) \pm S \ln\left(\frac{t}{t_0}\right) \tag{1}$$

where S is the time-dependent coefficient (or viscosity coefficient) and the plus or minus sign describes whether M is increasing or decreasing with time. In general, the viscosity of a real system of particles depends on a number of parameters, such as the reversal mechanism, interparticle interactions, particle volume, anisotropy field and easy axis distributions[1,2]. Moreover, it is a function of the applied field H and the temperature T. At a constant temperature, S increases with field, up to a maximum close to the coercive field (H_c), followed by a monotonic decrease as H is further increased [3].
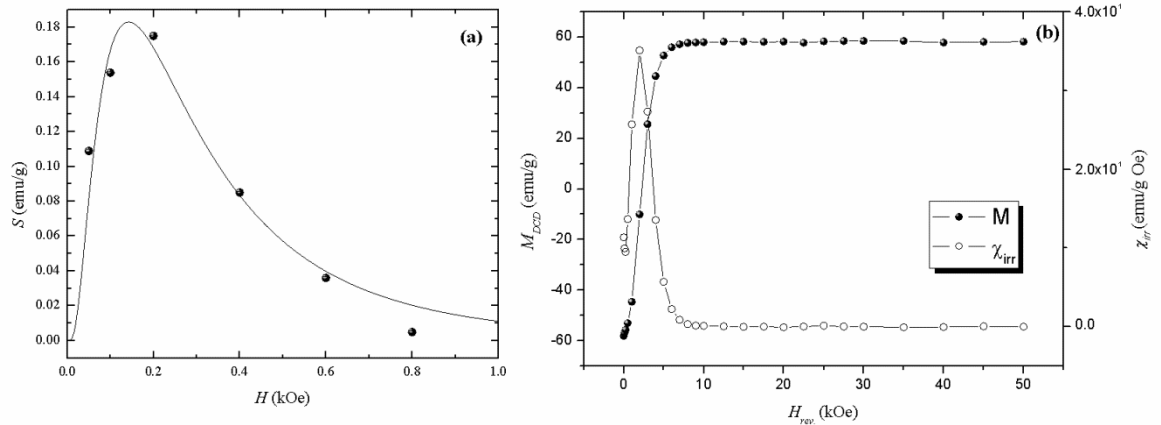
3

Figure S4. (a) Field dependence of magnetic viscosity for sample Zn75; (b) DCD remanent magnetization curve (full circles) and irreversible susceptibility (empty circles).

In a typical experiment, the sample is brought to a negative saturation field; then a reverse field is applied, and the time dependence of magnetization is measured. This experiment is repeated for several reverse fields around the coercivity value. By fitting the data to a logarithmic decay, the magnetic viscosity was estimated at different values of the reversed field. As an example, Figure S4 shows the field dependence of magnetic viscosity recorded at 5 K for sample Zn75 ($H_c \approx 0.2$ T).
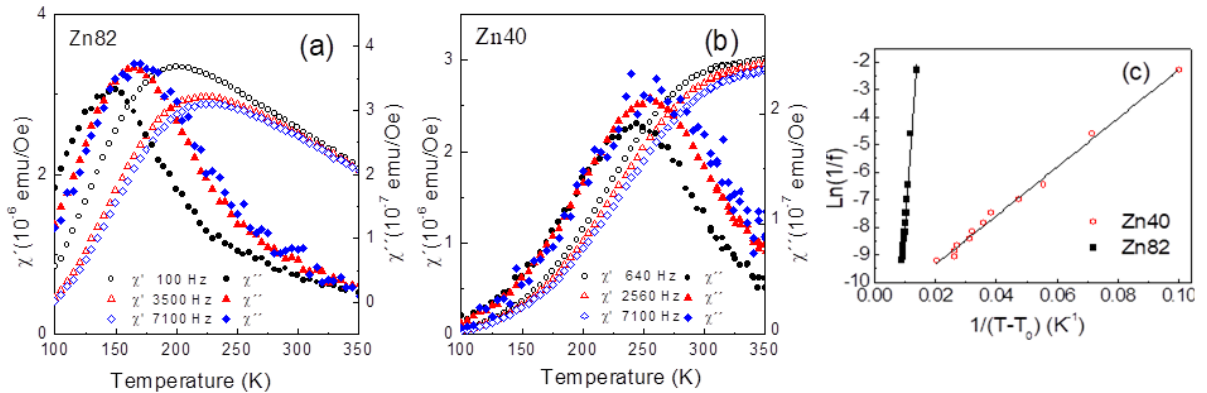

Figure S5. Real and imaginary part of the magnetic susceptibility of sample Zn82 (a) and Zn40 (b) samples, measured with driving field H_{ac} = 14 Oe.–Only selected frequencies are depicted. c) Frequency dependence of the χ'' peaks for Zn82 and Zn40 and the corresponding fitting with the Vogel-Fulcher law.

On the other hand, the fluctuation field, H_f, defined as an effective field which has the same effect on magnetization as that of thermal fluctuation energy, [4–6] can be calculated by combining the maximum value of magnetic viscosity (S_{max}) with the irreversible susceptibility (χ_{irr}), calculated at the same field:

$$H_f = \frac{S_{max}}{\chi_{irr}} \qquad (2)$$

The irreversible susceptibility has been obtained by remanent magnetization measured by DCD protocol. In particular, field of −5 T was applied for 10 s; then a reverse field ($H_{rev.}$) was applied, after 10 s it was switched off and the remanent magnetization (M_{DCD}) was measured. This was repeated, increasing the reverse field up to 5 T. (Figure S4(b) solid circles). The derivative of M_{DCD} gives us the irreversible susceptibility allowing the determination of H_f by equation (2). Finally, the fluctuation field can be used to estimate the activation volume ($V_{mag.}$) by the equation:

$$V_{mag} = \frac{k_B T}{M_s H_f} \qquad (3)$$

where k_B is the Boltzmann constant and the other parameters are those previously defined. The activation volume represents the smallest volume of material that reverses coherently in an event.[5]

Figure S5 shows the real (χ') and imaginary (χ'') part of the ac-magnetic susceptibility, measured at different frequencies (f) between 10 Hz and 10 kHz, applying an AC field of 14 Oe, for the samples Zn82 and Zn40. Fig 4-c presents the fit with the phenomenological Vogel-Fulcher law [7]:

$$\tau = \tau_0 \, \exp\left((E/k_B)/(T - T_0) \right) \qquad (4)$$

where E is the activation energy barrier, $\tau = 1/(2\pi f)$, and T_0 is a phenomenological parameter that provides a measure of the magnitude of the interactions. The fitting of the experimental data from sample Zn82 resulted in values $\tau_0 = 2(1) \ 10^{-11}$ s, $T_0 = 64(20)$ K and $E/k_B = 1500(50)$ K. When the Zn concentration decreases, the fitting of the frequency dependence peaks with Equation 4 gives non-physical values of τ_0, in the 10^{-5}- 10^{-7}s range. This indicates that these exchange coupled core/shell systems with larger magnetic anisotropy are outside of the applicability of the model.

References

[1]   R. Street, S.D. Brown, Magnetic viscosity , fluctuation fields , and activation energies, J. Appl. Phys. 6386 (2012) 1–6. https://doi.org/10.1063/1.358275.

[2]   K.D. Humfeld, A.K. Giri, A.S. Majestich, E.L. Venturini, Time dependent properties of iron nanoparticles, IEEE Trans. Magn. 37 (2001) 2194–2196.

[3]   D. Peddis, P.E. Jönsson, S. Laureti, G. Varvaro, Magnetic interactions: A tool to modify the magnetic properties of materials based on nanoparticles, 2014. https://doi.org/10.1016/B978-0-08-098353-0.00004-X.

[4]   R. Street, J.C. Woolley, A Study of Magnetic Viscosity, Proc. Phys. Soc. Sect. A. 62 (1949) 562–572. https://doi.org/10.1088/0370-1298/62/9/303.

[5]   V. Karanasos, I. Panagiotopoulos, D. Niarchos, H. Okumura, G.C. Hadjipanayis, Magnetic properties and granular structure of CoPt/B films, J. Appl. Phys. 88 (2000) 2740–2744.

[6]   D. Peddis, C. Cannas, G. Piccaluga, E. Agostinelli, D. Fiorani, Spin-glass-like freezing and enhanced magnetization in ultra-small CoFe2O4 nanoparticles, Nanotechnology. 21 (2010) 125705.

[7]   G. Lavorato, E. Winkler, A. Ghirri, E. Lima, D. Peddis, H.E. Troiani, D. Fiorani, E. Agostinelli, D. Rinaldi, R.D. Zysler, Exchange bias and surface effects in bimagnetic CoO-core/Co0.5Ni0.5Fe2O4-shell nanoparticles, Phys. Rev. B. 94 (2016) 054432. https://doi.org/10.1103/PhysRevB.94.054432.